Magnetic materials at finite temperatures: thermodynamics and combined spin and molecular dynamics derived from first principles calculations[1]

Markus Eisenbach[1], Dilina Perera[2], David P. Landau[2], Don M. Nicholson[3], Junqi Yin[4], Gregory Brown[5]

[1] National Center for Computational Sciences, Oak Ridge National Laboratory, Oak Ridge, TN 37831, USA
[2] Center for Simulational Physics, University of Georgia, Athens, GA 30602, USA
[3] Department of Physics, University of North Carolina, Asheville, NC 28804, USA
[4] National Institute for Computational Sciences, University of Tennessee, Oak Ridge, TN 37831, USA
[5] Department of Physics, Florida State University, Tallahassee, FL 32306, USA

E-mail: eisenbachm@ornl.gov

Abstract. We present a unified approach to describe the combined behavior of the atomic and magnetic degrees of freedom in magnetic materials. Using Monte Carlo simulations directly combined with first principles the Curie temperature can be obtained ab initio in good agreement with experimental values. The large scale constrained first principles calculations have been used to construct effective potentials for both the atomic and magnetic degrees of freedom that allow the unified study of influence of phonon-magnon coupling on the thermodynamics and dynamics of magnetic systems. The MC calculations predict the specific heat of iron in near perfect agreement with experimental results from 300K to above Tc and allow the identification of the importance of the magnon-phonon interaction at the phase-transition. Further molecular dynamics and spin dynamics calculations elucidate the dynamics of this coupling and open the potential for quantitative and predictive descriptions of dynamic structure factors in magnetic materials using first principles derived simulations.

1. Introduction

Understanding magnetic materials has been a long standing problem in condensed matter physics. While Hund's rule explains the magnetic moments of isolated atoms, it is the collective behavior of the electrons that is required to understand the interactions that lead to the formation of moments in bulk materials and their finite temperature behavior. In this paper we will concentrate on materials that can be mapped onto Heisenberg like models. Firstly we will describe our approach to calculating the energy of an arbitrary magnetic configuration from first principles using constrained density functional theory, then we will introduce the Monte

Carlo sampling methods we employ to calculate the partition functions for these materials and for calculating effective interactions that will be used in model simulations that allow us to explore the coupling of the magnetic and atomic degrees of freedom that are presently still beyond the capabilities of purely first principles approaches. In the last two sections we will use the parametrizations of the magnetic interactions to investigate the effects of coupling between the atomic and magnetic degrees of freedom on the thermodynamics and on the thermalization dynamics of the magnetization in iron systems.

2. Constrained First Principles Calculations

For the energy evaluation, we employ the first principles framework of density functional theory (DFT) in the local spin density approximation (LSDA). To solve the Kohn-Sham equations arising in this context, we use a real space implementation of the multiple scattering formalism. The details of this method for calculating the Green function and the total ground state energy $E[n(\vec{r}), \vec{m}(\vec{r})]$ are described elsewhere [1, 2]. Most importantly for the application in the hybrid Wang-Landau LSMS method, our Locally Self-consistent Multiple Scattering (LSMS) method allows the possibility of non-collinear magnetism [3].

The orientation $\hat{e}_i$ of the magnetic moment for each site is determined by

$$\hat{e}_i = \int_{\Omega_i} d\vec{r}\, \vec{m}_i(\vec{r}) / | \int_{\Omega_i} d\vec{r}\, \vec{m}_i(\vec{r})|. \tag{1}$$

Since an arbitrary arrangement is not a DFT ground state we will have to deal with a constrained general state as presented by Stocks *et al* [4, 5]. In the constrained local moment (CLM) model the LSDA equations are solved subject to a constraint

$$\int_{\Omega_i} \vec{m}_i(\vec{r}) \times \hat{e}_i d\vec{r} = 0 \tag{2}$$

that ensures that the local magnetizations lie along the directions prescribed by $\{\hat{e}_i\}$. The result is that, in order to maintain the specific orientational configuration, a local transverse constraining field must be applied at each site. The constraining field is obtained from the condition

$$\frac{\delta E^{con}[\{\hat{e}_i\}, \{\vec{B}_i^{con}\}]}{\delta \hat{e}_i} = 0 \tag{3}$$

applied to all sites and where E the generalized energy functional in the presence of the constraining field. Thus this method enables the calculation of the energies of arbitrary orientational states that will form the input of the following finite temperature calculations.

3. First Principles Wang-Landau Sampling

In the preceding section we described how we can calculate the constrained ground state energy $E(\{\hat{e}_i\})$ of an arbitrary magnetic ordering. In the approximation we employ in this paper, this represents the energy of a point in the system's phase space that is described by this set of magnetization directions $\{\hat{e}_i\}$. As we are interested in the thermodynamics of this system our goal is to calculate the partition function of this system of N sites:

$$Z(T) = \int_{S_2^N} e^{-E(\{\hat{e}_i\})/(k_B T)} d^{2N}\{\hat{e}_i\} \tag{4}$$

Even if atomic motions are not taken into account this represents a $2N$ dimensional integral over all possible moment directions, that in general can not be evaluated efficiently with standard numerical integration techniques. Also the energy calculation inside the integrand is orders of

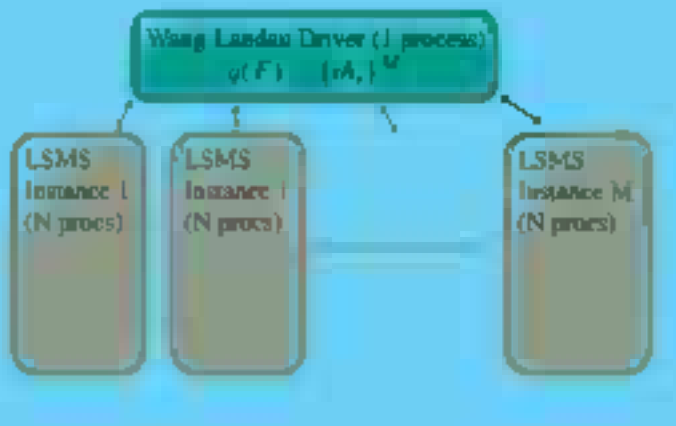

Figure 1. Parallelization strategy of the combined Wang-Landau/LSMS algorithm. The Wang-Landau process generates random spin configurations for M walkers and updates a single density of states $g(E)$. The energies for these N atom systems are calculated by independent LSMS processes. This results in two levels of communication, between the Wang-Landau driver and the LSMS instances, and the internal communication inside the individual LSMS instances spanning N processes each.

magnitude more computationally expensive than a simple Ising or Heisenberg model. In the next two subsections we will first describe the direct combination of the first principles energy calculation with a Monte Carlo sampling algorithm and then we will describe the fitting of model parameters in a way that will allow the construction of effective models that incorporate complex spin-spin interactions that depend on the atomic environment.

The Wang-Landau method [6, 7] has proven itself as a very efficient method to calculate the density of states $g(E)$ by flat energy histogram sampling of a system's phase space. This allows the partition function to be written as a one dimensional integral:

$$Z(T) = \int g(E) e^{-E/(k_B T)} dE \tag{5}$$

We have combined the Wang-Landau algorithm with the first principles LSMS method described above in a very efficient highly scalable parallel code (WL-LSMS) [8]. The WL-LSMS code uses a hybrid parallelization scheme. At the top level, the code parallelizes over concurrent random walkers, where we use a master-slave scheme, with a master that accumulates the density of states of the system, and the slaves that execute the random walks, each running its own instance of the LSMS method. The second parallelization level is the LSMS portion of the code, where domain decomposition is used with one atom per processing core. In typical production runs, the WL method would use a few hundred concurrent walkers, and the LSMS portion would be parallelized over up to a few thousand processing cores. The method hence will scale to hundreds of thousands or millions of processing cores. The schematics of the parallelization structure are shown in fig. 1.

4. Curie Temperature of Fe and Fe_3C

Utilizing the methods and algorithm described above for WL-LSMS we calculated the Curie temperatures of bulk bcc iron and cementite (Fe_3C) [9]. For the underlying LSMS calculations the atoms are placed on lattices with lattice parameters corresponding to the experimental room temperature values ($5.42a_0$ for bcc iron), and the local interaction zone has a radius of $11.5a_0$. The self-consistently converged potentials for the ferromagnetic ground states were used for all the individual frozen-potential energy calculations in the combined Wang-Landau/LSMS algorithm. The calculation was performed by randomly choosing a site in the supercell and randomly picking a new moment direction. We chose as convergence criterion for the Wang-Landau density of states the convergence of Curie temperature. Using the density of state thus

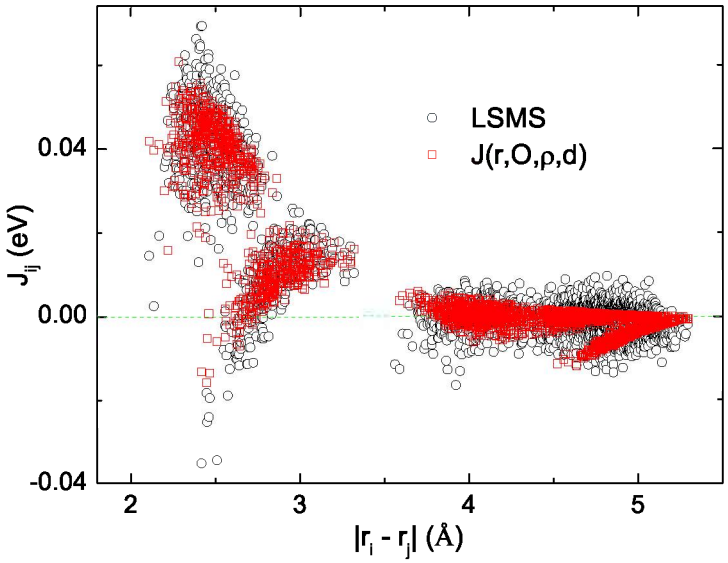

Figure 2. Pair exchange parameters J_{ij} calculated for all pairs (up to fifth nearest neighbor) in a 128 atom cell using the method described in the text (black circle) (equation 7) for a representative configuration (positions and spins) of BCC iron near T_c. The values for each pair is also shown as approximated by the function described in the text, $J(r, O, \rho, d)$ (red squares) (equation 13).

obtained we can calculate the specific heat. The peak in the specific heat allows us to identify the Curie temperature to be 980K for iron, in good agreement with the experimental value of 1050K. The Curie temperature obtained for Fe_3C is 425K which again is in good agreement with the experimental value of 480K. Note that compared with both experimental and model results the specific heat does not show the expected gradual rise below T_c but exhibits a sudden divergence whereas the high temperature behavior has the qualitatively correct behavior. This peculiarity is an artifact of the convergence criterion we have chosen for the Wang-Landau DOS. The method will first discover the high DOS areas and gradually explore the lower lying regions. To limit the expense of the calculation, it was terminated when no further changes in T_c were observed. This will yield good values for the DOS at energies that correspond to the transition temperature and above. Conversely, for lower energies the DOS will be far from convergence, resulting in the wrong qualitative behavior of thermodynamic properties calculated below T_c. A full convergence of the DOS for lower energies would have required an order of magnitude more samples, which would have made this calculation impractical on the computer resources currently available.

5. Fitting Model Parameters for Monte Carlo and Spin Dynamics Simulations

The procedure used to extract exchange parameters from first principles calculations is proposed in Ref. [10]. Considering a $4 \times 4 \times 4$ BCC lattice with thermal displacements generated using the Finnis-Sinclair potential [11] near the transition temperature, for each atom pair at site i and j within the first five shells (58 pairs for each atom), we calculate the total energy E^{ij} for specifically chosen moment orientaions on the sites i and j. A Heisenberg type of Hamiltonian is used to approximate the LSMS energies we obtained,

$$\begin{aligned} \mathcal{H} &= -\sum_{i<j} J_{ij}\vec{e}_i \cdot \vec{e}_j \\ &= -\sum_{k;k\neq i} J_{ik}\vec{e}_i \cdot \vec{e}_k - \sum_{k;k\neq j} J_{jk}\vec{e}_j \cdot \vec{e}_k \\ &\quad - \sum_{k<l;k,l\neq i,j} J_{kl}\vec{e}_k \cdot \vec{e}_l - J_{ij}\vec{e}_i \cdot \vec{e}_j \end{aligned} \tag{6}$$

where $\vec{e}_i$ is a unit vector for the atomic spin at site i. Then the exchange interaction parameter J_{ij} can be evaluated by considering 4 pair configurations for ($\vec{e}_i$, $\vec{e}_j$): ($\hat{z}$, $\hat{z}$), (-$\hat{z}$, $\hat{z}$), ($\hat{z}$, -$\hat{z}$), (-$\hat{z}$, -$\hat{z}$), for a total of $14848 = 4 * 128 * 58/2$ spin configurations, with corresponding energies E^{ij}, $E^{\bar{i}j}$, $E^{i\bar{j}}$, $E^{\bar{i}\bar{j}}$ as follows

$$J_{ij} = \frac{1}{4}\left(E^{ij} + E^{\bar{i}\bar{j}} - E^{\bar{i}j} - E^{i\bar{j}}\right). \tag{7}$$

Values of J_{ij} pairs are shown in Fig. 2. The large fluctuations indicate the instantaneous local magnetic moments become very inhomogeneous in the presence of displacements, and near the T_c the displacements are large, e.g., fluctuations in first nearest neighbor separations exceed the separation of second nearest neighbors, resulting in exchange parameters that depend on the local environment in a complicated manner that cannot be captured by a simple separation dependent interaction.

Note that one of the assumptions of our formula is that the Hamiltonian can be written in terms of pair-spin interactions. To eliminate the effect of the higher order terms, it is important that the energy calculation is performed in a background paramagnetic spin configuration (generated by randomly assigning spin directions) so that the cavity fields for the atoms considered are close to zero. As a tradeoff, the resulting J values could contribute to the underestimation of the magnetization in the ferromagnetic states [10], where effective many site interactions are becoming more important. We also investigated the direct least-square fitting of a representative set of LSMS energies to a Heisenberg model [12]; the data generally agree with the above procedure but with much larger variances.

6. Monte Carlo Simulations Combining Magnetic Excitations with Atomic Motion

In Ref. [10], we presented a parametrization of the exchange interaction for each shell as a function of the atomic separation, local volume, and local displacement. In general, the local atomic environment can also be described in terms of quantities already used in classical force fields, e.g., the density function employed in embedded-atom potentials is related to the coordination of the atom. To make the model applicable to molecular dynamics simulations, after comparing several popular iron potentials [11, 16, 17, 19], we re-parameterize the exchange parameter using the magnetic potential proposed by Dudarev and Derlet [19], which is given by

$$E^{\text{eam}} = \sum_i F[\rho_i] + \frac{1}{2}\sum_{ij, i\neq j} V(r_{ij}) \tag{8}$$

where the magnetic embedded function follows

$$F[\rho_i] = -A\sqrt{\rho}_i - \frac{B}{\ln 2}(1-\sqrt{\rho}_i)\ln(2-\rho_i)\Theta(1-\rho_i) \tag{9}$$

where Θ is the step function, the embedded density is $\rho_i = \sum_{j,i\neq j} f(r_{ij})$, and the pairwise functions for the density and pair interaction are defined as

$$\begin{aligned} f(r) &= \sum_{n=1}^{N^f} f_n (r - r_n^f)^3 \Theta(r - r_n^f) \\ V(r) &= \sum_{n=1}^{N^V} V_n (r - r_n^V)^3 \Theta(r - r_n^V) \end{aligned} \tag{10}$$

and parameters for $f(r)$ and $V(r)$ are listed in Table 1. One of the important reasons we choose the Dudarev-Derlet potential is that its pair density function is relatively short-range, and hence can better represent the local geometric properties.

Table 1. Parameters for the Dudarev-Derlet [19] potential.

A	3.527586256672234	r_n^V	V_n ($N^V = 6$)
B	1.642855167616477	4.1	$1.7533861115604772\times10^{-3}$
r_n^f	f_n ($N^f = 4$)	3.8	-0.9321219572059338
3.0	0.5055681753757052	3.5	1.696463955030590
2.86	-0.4255552831136833	3.2	0.6638478725109788
2.73	-0.5629408109339820	2.9	-1.914559267568704
2.6	0.4318530885665762	2.6	3.193687184255540

Considering that pairs of atoms from different shells share different numbers of neighbors and $f(r)$ measures the "neighborness" for each pair, we define the "overlapness" of atom i and j as

$$O_{ij} = \sum_{k,k\neq i,j} f(r_{ik})f(r_{jk}) \tag{11}$$

where the index k runs through the remaining atoms. The quantity O can statistically distinguish atom pairs from different shells, hence is a good parameter to represent the shell.

Similarly, the density ρ_i is a measure of the coordination of the atom i that depends on the positions of neighboring atoms. Therefore, it strongly correlates with the local volume which is defined as the volume of the Voronoi polyhedra formed by the surrounding atoms. In fact, the two quantities are inversely proportional. There is a small spread in the distribution, but overall, ρ is a good substitute for the local volume. Since the relative displacement from the perfect BCC structure results a force acting on the atom, we can express the local displacement variable with a force related term defined as

$$d_i = \sum_{k,k\neq i} |\vec{F}_{ik} \cdot \vec{r}_{ik}| \tag{12}$$

With only the separation distance as the parameter, the fitting is statistically significant up to the cubic term [10]. We choose a cutoff radius to bound the r term. After exhausting combinations of above explanatory variables and keeping terms that are significant in statistical tests, our model $J(r, O, \rho, d)$ for the exchange interaction between atom i and j follows,

$$\begin{aligned} J(r, O, \rho, d) = J_{ij}^{\text{eff}} = &(3.0035724 \times 10^{-3}\rho - 7.6680166 \times 10^{-7}d^2 \\ &+ 4.1178080 \times 10^{-4})(5.5 - r_{ij})^3\Theta(5.5 - r_{ij}) \\ &+ (8.1213771 \times 10^{1}r_{ij} - 1.9304247 \times 10^{1}r_{ij}^2 \\ &+ 1.4927816r_{ij}^3 + 9.8187830 \times 10^{-4}d^2 \\ &- 1.1340527 \times 10^{2} - 3.5371412 \times 10^{2}O_{ij} \\ &+ 3.9653967 \times 10^{4}O_{ij}^2)O_{ij} \end{aligned} \tag{13}$$

where $\rho = \rho_i + \rho_j$ and $d = d_i + d_j$. In Fig. 2, we plot J values from LSMS calculations and fitted values from our model for comparisons. The goodness-of-fit is about 0.92. Since the cutoff of $f(r)$ is at 3Å, $J^{\text{eff}}(r, O, \rho, d)$ is bound by the O at 6Å. Our Hamiltonian is in the form,

$$\mathcal{H} = -\sum_{i<j} J_{ij}^{\text{eff}}(\vec{e}_i \cdot \vec{e}_j - \langle \vec{e}_i \cdot \vec{e}_j \rangle) + E^{\text{eam}} \tag{14}$$

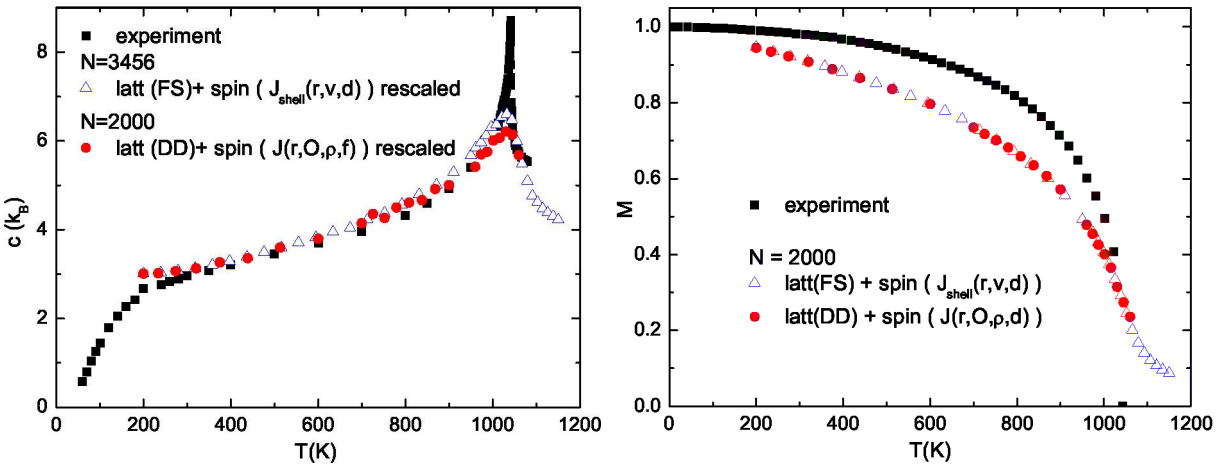

Figure 3. Comparison of specific heat and magnetization for experimental results[13, 14, 15], $J_{\rm shell}(r,v,d)$ [10] and $J(r,O,\rho,d)$ models. The Finnis-Sinclair (FS) potential is used with $J_{\rm shell}(r,v,d)$ model for a $12\times12\times12$ supercell, and the Dudarev-Derlet (DD) potential with $J(r,O,\rho,d)$ model for a $10\times10\times10$ supercell. The specific heat data from model calculations are rescaled according to Eq. 15.

We subtract the spin-spin correlation $\langle\vec{e}_i\cdot\vec{e}_j\rangle$ to correct the double counting of the ferromagnetic energy and obtain the same average energy as in $E^{\rm eam}$ potential. In practice, the correlation term is estimated self-consistently, and usually is converged during the process of equilibrating spins in Monte Carlo simulations. Since the parametrization of $J^{\rm eff}$ is based on quantities already employed in embedded-atom potentials, the model is a natural augmentation of the existing iron potentials, and is applicable to molecular dynamics simulations.

The specific heat for a $10\times10\times10$ supercell with Monte Carlo generated thermal displacements is calculated using the $J(r,O,\rho,d)$ model. The $\frac{3}{2}k_B$ contribution from the kinetic degree of freedom is added. Therefore, at zero temperature, the specific heat goes to $4k_B$ with $1k_B$ coming from the classical spin contribution. For small spin numbers ($S<\frac{7}{2}$), there is a discrepancy between classical and quantum calculations even at finite temperatures [18]. To obtain the corresponding quantum specific heat, a scaling factor $f=c_{\rm quantum}/c_{\rm classical}$ for the spin contribution was given by Körmann *et al.* [18] as follows,

$$f(t,s)=\left(\frac{2t_s/t}{e^{t_s/t}-e^{-t_s/t}}\right)^2 \qquad (15)$$
$$1/t_s=0.54S+0.54$$

where $t=T/T_c$ and $S=1.1$ for iron. For comparisons, in Fig. 3, we plot the scaled specific heat and magnetization for our model, as well as the experimental data [13, 14, 15] and results from Ref. [10] in which a similar $J_{\rm shell}(r,v,d)$ model was used. The magnetization curves of the two models overlap with each other, and the small discrepancy near specific heat peaks is simply due to the finite size effect in the simulation near the transition. The generalized shell-independent model agrees with $J_{\rm shell}(r,v,d)$ model within error bars, and can reproduce iron's specific heat from near T_c down to about $400K$. It also confirms our previous estimate of the spin-lattice contribution to the specific heat for BCC iron, which is significant near the T_c.

7. Combining Molecular Dynamics and Spin Dynamics Calculations

As shown in the preceding section, Monte Carlo is an ideal approach for effectively exploring the phase space and revealing the thermodynamic behavior of the system. However, due to the inherent stochastic nature of the sampling, MC methods are incapable of describing the time-dependent properties governed by the deterministic equations of motion (EOM). To gain qualitative insight into the dynamic behavior of the system, one needs to numerically solve the EOM and obtain the phase space trajectories in "real" time.

To adapt our coupled spin-lattice approach into a dynamical simulational model, we incorporate kinetic energy into Eq. 14 and obtain the extended Hamiltonian [20, 21]

$$\mathcal{H} = \sum_{i=1}^{N} \frac{m{\mathrm{v}_i}^2}{2} + E^{\mathrm{eam}} - \sum_{i<j} J(r_{ij}) \left(\vec{e}_i \cdot \vec{e}_j - 1\right) \quad , \tag{16}$$

where m is the mass of an atom and $\{\vec{v}_i\}$ are the velocities. For simplicity, we have replaced the spin-spin correlation $\langle \vec{e}_i \cdot \vec{e}_j \rangle_T$ by 1. In addition, J_{ij}^{eff} has been replaced by a simple pairwise representation, $J(r_{ij})$. [20]

The EOM governing the dynamics of the phase variables $\{\vec{r}_i\}$, $\{\vec{v}_i\}$ and $\{\vec{e}_i\}$ are given by

$$\frac{d\vec{r}_i}{dt} = \vec{v}_i \quad , \qquad \frac{d\vec{v}_i}{dt} = \frac{\vec{f}_i}{m} \qquad \text{and} \qquad \frac{d\vec{e}_i}{dt} = \frac{1}{\hbar S_i} \vec{H}_i^{eff} \times \vec{e}_i \quad , \tag{17}$$

where $\vec{f}_i = -\nabla_{\vec{r}_i} \mathcal{H}$ is the interatomic force and $\vec{H}_i^{eff} = \nabla_{\vec{S}_i} \mathcal{H}$ is the effective field, respectively. Although the spin lengths $\{S_i\}$ are not considered as phase variables, they are dynamically varied according to the local atomic environment via a regression relation [22] between the magnetic moment and the embedded density ρ_i of the Dudarev-Derlet potential.

The goal of the combined molecular and spin dynamics (MD-SD) approach is to numerically integrate the EOM starting from a given initial configuration. To achieve the highest possible numerical accuracy and stability, we use an advanced integration algorithm based on the second order Suzuki-Trotter (ST) decomposition for non-commuting operators [23, 24, 25].

7.1. Phonon-Magnon Interactions

MD-SD approach provides us with a unified framework for investigating the collective excitations at finite temperatures and explore the implications of the spin-lattice coupling. To characterize phonon and magnon modes in our model, we calculate dynamic structure factors $S(\vec{q}, \omega)$ [25] for momentum transfer $\vec{q}$ and frequency transfer ω, for a $10 \times 10 \times 10$ simulation cell. EOM were integrated up to a total time of 1 ns using a timestep of 1 fs, with periodic boundary conditions imposed. Initial states for the time integration were drawn from the canonical ensemble using MC simulations.

Fig. 4 shows the transverse component of the spin-spin dynamic structure factor at the room temperature $T = 293\,\mathrm{K}$, for $\vec{q} = (0.88\,\text{Å}^{-1}, 0, 0)$. For comparison, we have also shown the results obtained from pure spin dynamics (SD) simulations with atoms fixed at perfect BCC lattice positions. With the inclusion of lattice vibrations, we observe that the peak shifts to lower frequencies. Moreover, half-width of the peak increases while the amplitude decreases, which are clear indications of the damping of the spin waves.

Fig. 5 shows the longitudinal spin-spin dynamic structure factor at $T = 800\,\mathrm{K}$ for $\vec{q} = (0.22\,\text{Å}^{-1}, 0, 0)$; *with* [subset (a)] and *without* [subset (b)] the influence of the phonons. Surprisingly, the additional excitation peak we observe in the subset (a) at $\omega \approx 7\,\mathrm{meV}$ coincides with the peak position of the density-density dynamic structure factor (shown in the inset) for the same $\vec{q}$. This, undoubtedly proves the existence of coupled phonon-magnon modes.

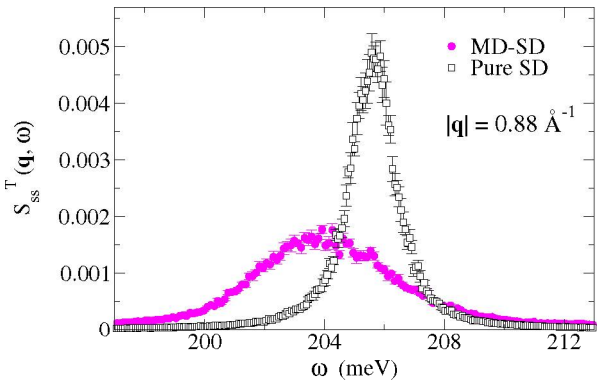

Figure 4. Transverse component of the spin-spin dynamic structure factor $S^T_{ss}(\vec{q},\omega)$ at $T = 293$ K for $\vec{q} = (0.88\,\text{Å}^{-1}, 0, 0)$, for a $10\times10\times10$ simulation cell. Full circles represent data obtained from combined molecular and spin dynamics (MD-SD) while open squares show pure spin dynamics (SD) results.

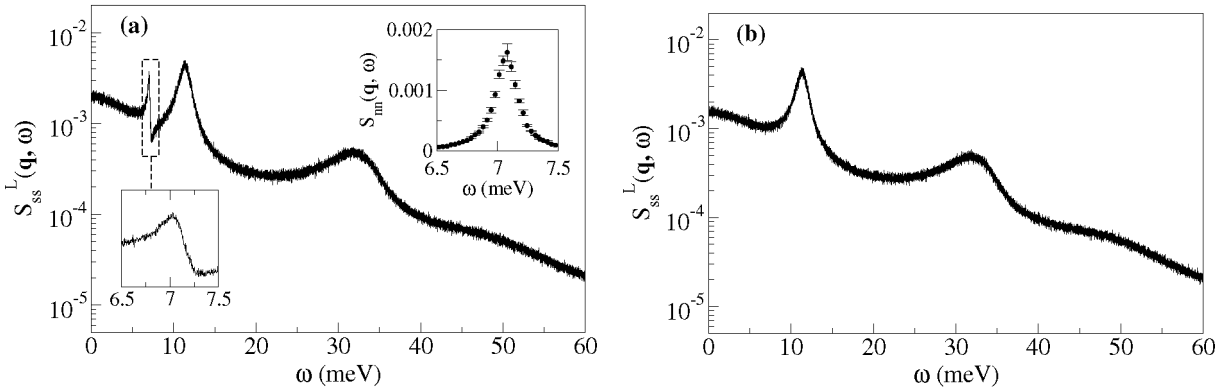

Figure 5. Longitudinal component of spin-spin dynamic structure factor $S^L_{ss}(\vec{q},\omega)$ at $T = 800$ K for $\vec{q} = (0.22\,\text{Å}^{-1}, 0, 0)$ for a $10 \times 10 \times 10$ simulation cell. (a) Combined molecular and spin dynamics simulations (b) Pure spin dynamics simulations on a rigid lattice. Inset of (a) shows the density-density dynamic structure factor for the same $\vec{q}$.

7.2. Modeling Spin-Orbit Interactions

Hamiltonian described by Eq. 16 suffers from a major deficiency in regard to accurately establishing the coupling between the lattice and the spin subsystems. Although the coordinate-dependent exchange interaction enables the exchange of energy between the two subsystems, it does not facilitate the transfer of angular momentum in a similar manner [20].

In conventional molecular dynamics, system temperature can be externally controlled via a thermostat coupled to the lattice degrees of freedom. In MD-SD formalism, controlling the lattice temperature, in principle, should allow the spin subsystem to thermalize and subsequently brought into equilibrium with the lattice subsystem. However, the conservation of spin angular momentum strictly prohibits the thermal excitation of the spin orientations, imposing an artificial entropic barrier between the two subsystems.

As the first step towards solving this issue, we identify that the "missing ingredient" in our model is a mechanism that incorporates spin-orbit coupling. Since the notion of orbital angular momentum ($\vec{L}$) does not exist in the MD-SD approach, one cannot introduce spin-orbit interactions directly into the Hamiltonian as an atomistic level abstraction of the form, $\mathcal{H}_{\text{SO}} \sim \vec{L}\cdot\vec{S}$. Therefore we model the underlying effects of spin-orbit coupling in terms of its emergent phenomenon, magnetocrystalline anisotropy.

In the bulk phase of 3d transition metals, crystal-field interaction largely surpasses spin-orbit coupling, leading to quenched orbital magnetic moments and negligibly small anisotropy energies

[27, 28]. However, in low symmetry environments such as surfaces and thin films, spin-orbit coupling is greatly enhanced [29, 30] due to the changes in the effective potential experienced by the electrons. Following the same argument, we claim that the lattice symmetry breaking that occurs due to phonons at finite temperatures may also strengthen spin-orbit coupling by a significant amount. Consequently, this will induce magnetic anisotropies locally on an atomic scale. Magnitudes and easy axes of these anisotropies are completely determined by the local atomic environment and change dynamically as the system evolves in time.

Expanding the anisotropy energy of the ith spin $\vec{S}_i$ in successive powers of its components we obtain

$$E_i^{\text{anis}}(S_{ix}, S_{iy}, S_{iz}) = \varepsilon \; + \; \sum_{\alpha} \kappa_\alpha S_{i\alpha} \; + \; \sum_{\alpha} \sum_{\beta} \lambda_{\alpha\beta} S_{i\alpha} S_{i\beta} \; + \; \sum_{\alpha} \sum_{\beta} \sum_{\gamma} \xi_{\alpha\beta\gamma} S_{i\alpha} S_{i\beta} S_{i\gamma} \; + \; \cdots , \tag{18}$$

where $\alpha, \beta, \gamma = x, y, z$. Coefficients of this expansion solely depend on symmetry of the local atomic environment surrounding the ith atom. Note that we have completely neglected the cubic anisotropy in bcc iron. Hence all anisotropy coefficients become identically zero as the atoms occupy perfect crystal lattice positions.

Ignoring the terms of third order and above, we write the anisotropic contribution to the Hamiltonian in the following concise form

$$\mathcal{H}_{\text{anis}} = -C_1 \sum_{i=1}^{N} \vec{K}_i \cdot \vec{S}_i - C_2 \sum_{i=1}^{N} \vec{S}_i^{\mathsf{T}} \cdot \mathbf{\Lambda}_i \cdot \vec{S}_i, \tag{19}$$

where C_1 and C_2 are constants. To establish the connection to the local environment, we write vector $\vec{K}_i$ and tensor $\mathbf{\Lambda}_i$ in terms of the derivatives of a scalar function $\varrho_i(\{\vec{r}_k\})$ as

$$\vec{K}_i = \nabla_{\vec{r}_i} \varrho_i \quad , \qquad \mathbf{\Lambda}_i = \begin{pmatrix} \frac{\partial^2 \varrho_i}{\partial {x_i}^2} & \frac{\partial^2 \varrho_i}{\partial x_i \partial y_i} & \frac{\partial^2 \varrho_i}{\partial x_i \partial z_i} \\ \frac{\partial^2 \varrho_i}{\partial y_i \partial x_i} & \frac{\partial^2 \varrho_i}{\partial {y_i}^2} & \frac{\partial^2 \varrho_i}{\partial y_i \partial z_i} \\ \frac{\partial^2 \varrho_i}{\partial z_i \partial x_i} & \frac{\partial^2 \varrho_i}{\partial z_i \partial y_i} & \frac{\partial^2 \varrho_i}{\partial {z_i}^2} \end{pmatrix}. \tag{20}$$

Function $\varrho_i(\{\vec{r}_k\})$ is chosen such that its derivatives quantitatively reflect the local symmetry surrounding the ith atom. For convenience, we construct ϱ_i in a manner similar to which the embedded density ρ_i is defined in the embedded-atom formalism. That is, $\varrho_i = \sum_{j(j\neq i)} \phi(r_{ij})$, where $\phi(r_{ij})$ is a pairwise function with a short range cutoff distance. This particular functional form guarantees that under perfect crystalline symmetry, $\nabla_{\vec{r}_i} \varrho_i$ and the off-diagonal elements of $\mathbf{\Lambda}_i$ vanish. Although the diagonal elements of $\mathbf{\Lambda}_i$ are non-zero, they become identical, which only leads to a constant shift in energy. $\phi(r_{ij})$ was chosen to be a rapidly decaying function with an arbitrary form of $\phi(r_{ij}) = (1 - r_{ij}/r_c)^4 \exp(1 - r_{ij}/r_c)$, where the cutoff distance $r_c = 3.5$ Å lies between the second and the third nearest neighbor distances. Fourth order polynomial contribution ensures that all interatomic forces that arise due to the coordinate-dependence of $\mathcal{H}_{\text{anis}}$ smoothly go to zero at the cutoff distance.

Eq. 16 combined with the anisotropy terms in Eq. 19 constitutes a complete MD-SD model that fully couples the translational and spin degrees of freedom. To show that our refined model eradicates the shortcomings of the original approach, we perform NVT simulations to investigate the thermal relaxation of a $10 \times 10 \times 10$ lattice. Anisotropy coefficients C_1 and C_2 were arbitrarily set to 2.0 and 1.0, respectively. Initially, all atoms were arranged on a perfect BCC lattice with zero velocities while all spins were aligned in the z direction. Lattice temperature was explicitly controlled by replacing the dynamical equation for the velocities with the stochastic Langevin equation [31]

$$m \frac{d\vec{v}_i}{dt} = -\eta \vec{v}_i + \vec{f}_i + \vec{R}_i(t), \tag{21}$$

where η is the damping constant and $\vec{R}_i(t)$ is the random force that satisfies the condition $\langle R_{i\alpha}(t)R_{j\beta}(t')\rangle = 2\eta k_B T\delta(t-t')\delta_{ij}\delta_{\alpha\beta}$, with T being the temperature and $\alpha,\beta = x, y, z$. Time evolution of the spins is governed by the conventional spin dynamics equation. That is, NO external torques were applied to the spins in order to control the spin temperature. Fig. 6 (upper panel) shows the time evolution of the instantaneous lattice temperature (T_L) and spin temperature (T_S) with target temperatures set to 300 K [subset (a)] and 800 K [subset (b)]. Subsets (c) and (d) show the net magnetization per atom for the same respective simulations. T_L was measured using the familiar average kinetic energy expression whereas for T_S we have used the formula developed by Nurdin et al. [32]

$$T_S = \frac{\sum_i |\vec{S}_i \times \nabla_{\vec{S}_i}\mathcal{H}|^2}{k_B \sum_i [\vec{S}_i \times \nabla_{\vec{S}_i}] \cdot [\vec{S}_i \times \nabla_{\vec{S}_i}]\mathcal{H}}. \tag{22}$$

As expected, we observe a gradual decrease in the magnetization accompanied by an increase in the spin temperature, as the spin subsystem loses angular momentum via the anisotropy terms in the Hamiltonian. Eventually, these quantities converge to their corresponding equilibrium values as the spin and lattice subsystems mutually reach the equilibrium with the thermostat. Moreover, we observe that the relaxation rate of the spin subsystem increases noticeably with the target temperature. As the thermostat temperature increases, thermal fluctuations of the atomic positions also increase. This would further intensify the locally induced anisotropies, hence leading to an increase in the relaxation rate.

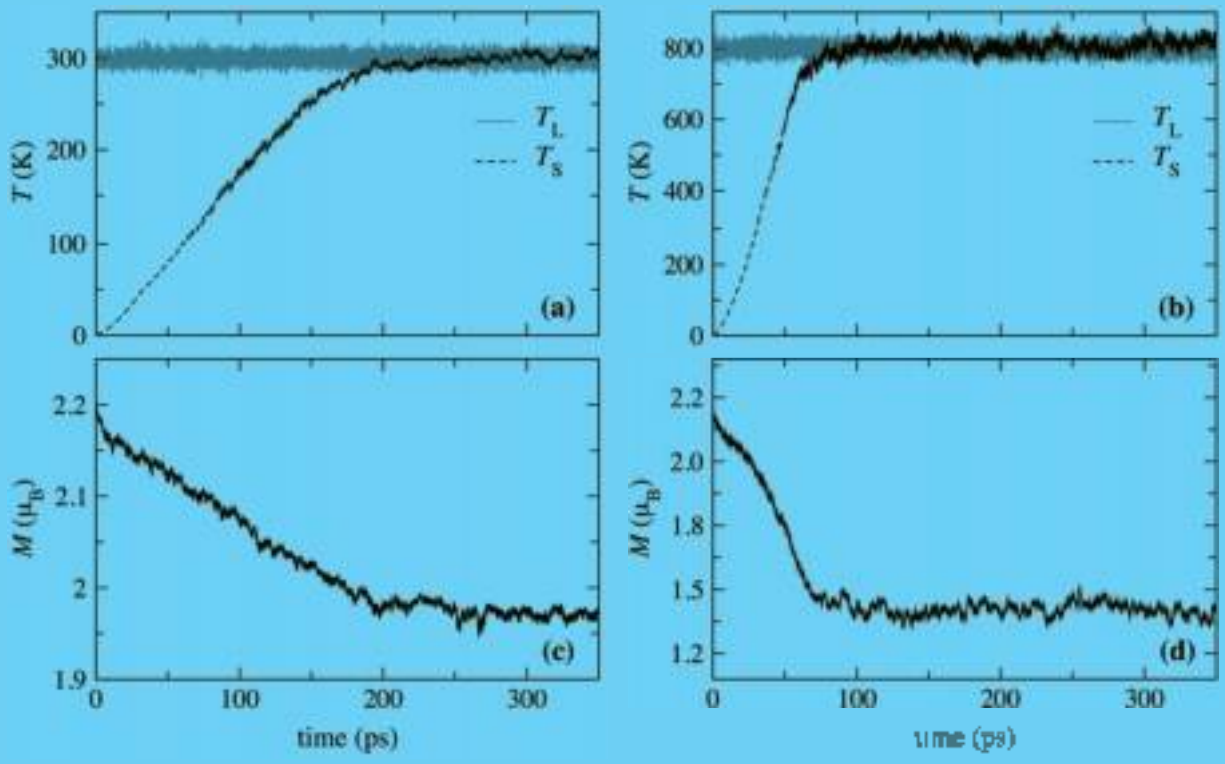

Figure 6. Thermalization of a $10 \times 10 \times 10$ simulation cell via lattice thermostats set to target temperatures 300 K [(a) and (c)] and 800 K [(b) and (d)]. Upper panel [(a) and (b)] shows the time evolution of the lattice temperature (T_L) and spin temperature (T_S) while the lower panel [(c) and (d)] shows the net magnetization per atom.

8. Conclusion

We have developed the capability to calculate thermodynamic properties of magnetic systems purely from first principles. While this direct first principles approach is still too computationally expensive to be applied as a routine method, we have demonstrated a method to use these first principles calculations to derive classical models that encapsulate the essential physics. These models allow us to explore material specific consequences of magnon-phonon coupling both on the equilibrium thermodynamics as well as on the dynamics of magnetic materials.

Acknowledgments

This work is sponsored by the U.S Department of Energy, Office of Science, Basic Energy Sciences, Materials Sciences and Engineering Division (*ab initio* and Monte Carlo) and by the *Center for Defect Physics*, an Energy Frontier Research Center (spin dynamics-molecular dynamics). This research used resources of the Oak Ridge Leadership Computing Facility at ORNL, which is supported by the Office of Science of the U.S. Department of Energy under Contract No. DE-AC05-00OR22725.

References

[1] Wang Y, Stocks G M, Shelton W A, Nicholson D M, Szotek Z and Temmerman W M 1995 *Phys. Rev. Lett.* **75** 2867
[2] Eisenbach M, Györffy B L, Stocks G M and Ujfalussy B 2002 *Phys. Rev. B* **65** 144424
[3] Stocks G M, Wang Y, Nicholson D M C, Shelton W A, Szotek Z, Temmerman W M, Harmon B N and Antropov V P 1996 *Mater. Res. Soc. Symp. Proc.* **408** 157
[4] Stocks G M, Ujfalussy B, Wang X, Nicholson D M C, Shelton W A, Wang Y, Canning A and Györffy B L 1998 *Philos. Mag. B 78* 665
[5] Ujfalussy B, Wang X, Nicholson D M C, Shelton W A, Stocks G M, Wang Y and Györffy B L 1999 *J. Appl. Phys.* **85** 4824
[6] Wang F and Landau D P 2001 *Phys. Rev. Lett.* **86** 2050
[7] Wang F and Landau D P 2001 *Phys. Rev. E* **64** 056101
[8] Eisenbach M, Zhou C-G, Nicholson D M, Brown G, Larkin J, Schulthess T C 2009 *SC09: Proceedings of the Conference on High Performance Computing, Networking, Storage and Analysis* ACM
[9] Eisenbach M, Nicholson D M, Rusanu A and Brown G 2011 *J. Appl. Phys.* **109** 07E138
[10] Yin J, Eisenbach M, Nicholson D M and Rusanu A 2012 *Phys. Rev. B* **86** 214423
[11] Finnis M W and Sinclair J E 1984 *Phil. Mag. A* **50** 45
[12] Yin J, Eisenbach M, Nicholson D M and Rusanu A 2013 *J. Appl. Phys* **113** 17E112
[13] Shacklette L W 1974 *Phys. Rev. B* **9** 3789
[14] White G K and. Minges M L 1997 *Int. J. Thermophys.* **18** 1269
[15] Crangle J and Goodman G M 1971 *Proc. R. Soc. Lond. A* **321** 477
[16] Finnis M W and Sinclair J E 1986 *Phil. Mag. A* **53** 161
[17] Mendelev M I, Han S, Srolovitz D J, Ackland G J, Sun D Y and Asta M 2003 *Phil. Mag. A* **83** 3977
[18] Körmann F, Dick A, Hickel T and Neugebauer J 2010 *Phys. Rev. B* **81** 134425
[19] Dudarev S L and Derlet P M 2005 *J. Phys.:Condens. Matter* **17** 7097
[20] Ma P W, Woo C H and Dudarev S L 2008 *Phys. Rev. B* **78** 024434
[21] Perera D, Landau D P, Nicholson D M, Malcolm Stocks G, Eisenbach M, Yin J and Brown G 2014 *Journal of Applied Physics* **115** 17D124
[22] Derlet P M and Dudarev S L 2007 *Prog. Mater. Sci.* **52** 299
[23] Krech M, Bunker A and Landau D P 1998 *Comput. Phys. Commun.* **111** 1
[24] Omelyan I P, Mryglod I M and Folk R 2001 *Phys. Rev. Lett.* **86** 898
[25] Perera D, Landau D P, Nicholson D M, Malcolm Stocks G, Eisenbach M, Yin J and Brown G 2014 *J. Phys.: Conf. Ser.* **487** 012007
[26] Aharoni A 2000 *Introduction to the theory of ferromagnetism* (New York: Oxford University Press)
[27] Daalderop G H O, Kelly P J and Schuurmans M F H 1990 *Phys. Rev. B* **41** 11919
[28] Skomski R 2008 *Simple Models of Magnetism* Oxford Graduate Texts (New York: Oxford University press)
[29] Wang D S, Wu R and Freeman A J 1993 *Phys. Rev. B* **47** 14932
[30] Lessard A, Moos T H and Hübner W 1997 *Phys. Rev. B* **56** 2594
[31] Kubo R 1966 *Rep. Prog. Phys.* **29** 255
[32] Nurdin W B and Schotte K D 2000 *Phys. Rev. E* **61** 3579